Analytica Chimica Acta 1203 (2022) 339721

Contents lists available at ScienceDirect

Analytica Chimica Acta

journal homepage: www.elsevier.com/locate/aca

Plasmon-enhanced near-infrared fluorescence detection of traumatic brain injury biomarker glial fibrillary acidic protein in blood plasma

Peng Zheng [a], Sujan Kasani [a], Weirui Tan [b], Jennifer Boryczka [b], Xuefei Gao [a], Feng Yang [c], Nianqiang Wu [a, b, *]

[a] Department of Mechanical and Aerospace Engineering, West Virginia University, Morgantown, WV, 26506-6106, United States
[b] Department of Chemical Engineering, University of Massachusetts Amherst, Amherst, MA, 01003-9303, United States
[c] Industrial and Management Systems Engineering Department, West Virginia University, Morgantown, WV, 26506, United States

HIGHLIGHTS

- Developed a plasmonic near-infrared fluorescent biosensor.
- Unveiled excitation enhancement responsible for fluorescence signal amplification.
- Enabled detection of a low level of traumatic brain injury protein biomarker in blood plasma.

GRAPHICAL ABSTRACT

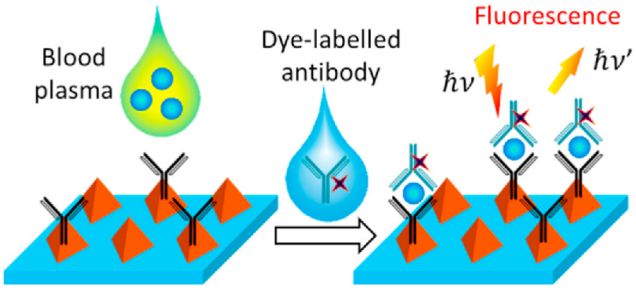

ARTICLE INFO

Article history:
Received 17 December 2021
Received in revised form
20 February 2022
Accepted 9 March 2022
Available online 11 March 2022

Keywords:
Biosensor
Glial fibrillary acidic protein
Traumatic brain injury
Fluorescence
Surface plasmon resonance
Nanoarray

ABSTRACT

An ultrasensitive plasmonic near-infrared fluorescent biosensor substrate has been developed for detection of glial fibrillary acidic protein (GFAP) biomarker in blood plasma, an important protein biomarker of traumatic brain injury (TBI). To minimize the interference from blood plasma sample matrix, a near-infrared fluorophore in the first biological transparency window is used in the biosensor. To amplify the fluorescence signals, a plasmonic gold nanopyramid array has been coupled to the fluorophore. Finite-difference time-domain simulation reveals that the excitation enhancement is primarily responsible for the fluorescence enhancement owing to the intense local electric field excited on the corners and edges. As a result, this biosensor exhibits a lower limit of detection of 0.6 pg/mL toward detection of GFAP in blood plasma.

1. Introduction

Traumatic brain injury (TBI) accounts for about 30% of all injury deaths according to Centers for Disease Control and Prevention [1]. While early treatment could effectively reduce short- and long-term adverse clinic outcomes, rapid diagnosis of TBI remains highly challenging due to lack of rapid, objective, and quantitative method for TBI screening; and the symptoms may not appear until days or even weeks. Glasgow Coma Scale is the current prevailing TBI screening method, which are subjective tests of speech, cognition, neuropsychological behaviors. It causes large errors for

* Corresponding author. Department of Mechanical and Aerospace Engineering, West Virginia University, Morgantown, WV, 26506-6106, United States.
E-mail address: nianqiangwu@umass.edu (N. Wu).

https://doi.org/10.1016/j.aca.2022.339721
0003-2670/

mild and moderate TBI [2]. In contrast, quantification of diagnostic biomarkers is capable of revealing the full spectrum of biological disorders from initial manifestations to terminal stages [3,4]. Currently, widely acknowledged TBI biomarkers in blood include glial fibrillary acidic protein (GFAP), ubiquitin carboxyl-terminal hydrolase L1 (UCH-L1), S100-β, neuron-specific enolase (NSE) and etc. [5,6]. Among these biomarkers, the cut-off value of GFAP is extremely low (60 pg/mL) for mild TBI [7,8]. It remains a technical challenge in quantifying trace protein biomarkers in blood.

Enzyme-linked immunosorbent assay (ELISA) and Western blot are two common techniques for protein biomarker detection [9–11]. Both methods require professional staff and sophisticated instruments in a central laboratory; and they are time-consuming due to tedious operational procedures [10]. The typical ELISA assay time is around 3 h, and Western blot even takes a day to finish. Furthermore, most ELISA kits can only reach a limit of detection (LOD) of around 10 pg/mL for GFAP. Therefore, it is essential to develop rapid, sensitive, and quantitative tools for measurement of trace TBI protein biomarkers. Recently, electrochemical biosensors were developed for TBI biomarkers detection, but most of them were only demonstrated in PBS buffer [12–17] because electrochemical biosensors suffer from strong interference and biofouling in blood sample matrices. Recently, fluorescent biosensors have received increasing attention [18–22]. However, most of current fluorescent biosensors transduce visible-light fluorescence signals. Excitation and emission of visible-light organic dye fluorophores in blood are subject to strong absorption of biomolecules such as bilirubin, oxy-hemoglobin and deoxy-hemoglobin, and suffer from interference from autofluorescence of amino acids and proteins in blood such as pyridoxine, retinol A, collagen, cholecalciferol, folic acid, and porphyrin [23–26]. To mitigate these problem, near-infrared (NIR) fluorophores that fall into the biological transparency windows are attractive for plasma, serum and whole blood sample matrices [27–29]. Nevertheless, NIR fluorophores usually exhibit a much less emission intensity as compared to the visible-light counterparts [30]. Because their molecular energy levels are more likely to overlap with other transitions, there is a higher chance of non-radiative energy transfer, reducing the fluorescence intensity. Fortunately, the two-step process nature of fluorescence involving excitation and emission offers numerous opportunities to enhance the brightness of NIR fluorophores by optimizing either the excitation, the emission, or both [31].

Plasmon has been reported to improve sensitivity of biosensors by enhancing fluorescence intensity [32–35]. There are two mechanisms for plasmon-enhanced fluorescence: excitation enhancement and emission enhancement [21,36–41]. The excitation enhancement of fluorescence is possible through both Förster resonance energy transfer (FRET) at close distances (~10 nm) and the Purcell effect at longer distances (10–50 nm). In the emission process, the probability that the excited fluorophore emits a photon is dependent on competition between radiative and non-radiative decay processes. This is represented by the quantum efficiency. Based on Fermi's golden rule, the spontaneous decay rate scales with the local density of optical states. Therefore, the emission enhancement could result from the increased local density of optical states induced by the plasmonic nanostructure. Unfortunately, while minimizing the mode volume in which the local electric field is confined could maximize the excitation enhancement, it also introduces strong energy loss channels, which could significantly decrease the quantum efficiency and end up compromising the overall fluorescence intensity. This phenomenon is especially obvious for open plasmonic metallic nanostructures, where the excitation enhancement is predominately responsible for the fluorescence enhancement [42–44]. In short, the plasmon-induced fluorescence enhancement is strongly dependent on the separation distance. At a short distance, plasmon is quenched by plasmon. At a long distance, the plasmonic enhancement decays with the separation distance. The optimal separation distance for fluorescence enhancement generally falls into a range of 10–30 nm [39].

In this study, a NIR fluorescent biosensor is developed for detection of the GFAP biomarker. The NIR fluorophore used is Dylight 755, which is labelled on the GFAP antibody. It has a peak excitation and emission wavelength of 755 nm and 775 nm, respectively, with an intrinsic quantum efficiency of 11.9% [45], which is among the highest in NIR fluorophores. A gold nanopyramid array pattern is fabricated on the glass by nanosphere lithography [46,47] and used as the biosensing platform after functionalization with the capture antibody specific to GFAP. Notably, a portable fluorescence reader is used to conduct all the tests instead of a large-scale spectrofluorometer. Finite-difference time-domain (FDTD) simulation is implemented to unveil the origin of the fluorescence enhancement as well as to calculate the fluorescence enhancement factor.

2. Experimental methods

Chemicals and Materials. (3-Mercaptopropyl) trimethoxysilane (95%), BSA (bovine serum albumin), phosphate buffered saline tablets, monoclonal anti-glial fibrillary acidic protein antibody produced in mouse (G3893-.2 ML, ~50 kDa), glial fibrillary acidic protein human brain (345996-100UG, 50 kDa), sodium silicate solution (338443-1L), *N*-hydroxysuccinimide (NHS), and 1-ethyl-3-(3-(dimethylamino)-propyl) carbodiimide (EDC), were purchased from Sigma-Aldrich. (3-Triethoxysilyl) propylsuccinicanhydride (TEPSA) was purchased from Gelest. The IgG-free blood plasma was acquired from US Biological Life Science (P4252-56 Plasma, Human). Dylight 755 NHS Ester Microscale Antibody Labelling Kit and polystyrene microspheres with a diameter of 600 nm were bought from Thermo Scientific. Deionized (DI) water used for washing and reactions was produced by Milli-Q Millipore system (18.2 MΩ cm, Millipore Corp., Billerica, MA). Human Glial Fibrillary Acidic Protein ELISA Kit (abx050253) was purchased from Abbexa. All chemicals obtained from commercial vendors and were directly used without further purification.

Fabrication of Gold Nanopyramid Arrays. Au nanopyramid arrays were fabricated on glass slides (roughly 0.5 cm × 0.5 cm) by nanosphere lithography [48], as shown in Fig. S1. Prior to the fabrication, the glass slides were cleaned using acid piranha (the ratio of sulfuric acid to hydrogen peroxide is 3:1) at 90 °C for 1 h. Caution: acid piranha is very dangerous and needs to be handled with extreme care! They were subsequently rinsed with DI water, cleaned by ultrasonication three times in ethanol and DI water, respectively. After that, a monolayer of polystyrene beads was dip-coated on glass slides, which formed a periodic hexagonal pattern. Afterwards, a 5 nm thick titanium layer followed by a 250 nm thick gold layer were deposited onto the pattered substrate by e-beam evaporator (Kurt J Lesker, Model#LAB18), respectively. Next, the polystyrene beads were removed by ultrasonication in methanol and dried using compressed air. A hexagonally ordered Au nanopyramid array was obtained.

Coating a Thin Silica Film onto Gold Nanopyramid Array. Following the protocol reported [49], a thin layer of silica was conformationally grown on Au nanopyramid arrays. Specifically, the as-fabricated Au nanopyramid arrays were first incubated in the ethanolic solution of 2 mM (3-Mercaptopropyl) trimethoxysilane for 2 h. After rinsing with ethanol and DI water, the Au nanopyramid arrays were then incubated in a sodium silicate solution (1.5 wt%, pH 8–9) at 90 °C for 2 days. In the meanwhile, the Au film substrates were also coated with a thin layer of silica under the

same conditions as the control samples.

Labelling of Detection Antibody with Dylight 755. Following the protocol provided by Thermo Scientific, the detection antibody was initially labelled with Dylight 755. Specifically, the concentration of detection antibody was adjusted to 1 mg/mL in a PBS buffer solution. 8 μL of Borate Buffer (0.67 M) was then added to 100 μL of 1 mg/mL antibody in PBS. The mixed solution was further added to the Dylight Reagent vial containing 15 μg of Dylight 755 NHS ester powder. After thorough mixing, the solution was incubated at room temperature in dark for 1 h. To purify the Dylight-labelled antibody, the above solution was added to the purification resin and then centrifuged at 1000×*g* for 1 min. The obtained Dylight-labelled was stored at 4 °C in dark for future use.

Immobilization of Capture Antibody onto Nanoarrays. The silica-coated Au nanopyramid arrays were first incubated overnight in an ethanolic solution containing 100 mM TEPSA to achieve the carboxylic-modified surface. A PBS buffer solution containing 50 mM NHS and 200 mM EDC was used to activate the carboxylic groups. Subsequently, the Au nanopyramid arrays were incubated in a 20 μg/mL capture antibody solution overnight. The capture antibody-modified Au nanopyramid arrays were further incubated in a PBS buffer solution containing 1 mg/mL BSA blocker for 2 h to achieve high specificity. For all the interim steps, the PBS buffer solution was used to remove excessive chemical and biological reagents.

Characterization. The thin silica layer grown on Au film was characterized by ellipsometry (J. A. Woollam M − 2000U Ellipsometer), which gave a mean thickness of 2.4 nm from 3 independent samples. The Au nanopyramid arrays were imaged using a JEOL JSM-7600F scanning electron microscope (SEM). The reflection spectra of Au nanopyramid arrays were acquired by an Ocean Optics USB 4000 spectrometer. The fluorescence intensity of the biosensor was measured with a compact point-of-care (cPOC) fluorescence reader (cPoCLabFluo v2.3.0, LRE Medical GmbH, München, Germany), where the excitation wavelength was 755 nm, and the fluorescence emission wavelength was 775 nm.

Finite-Difference Time-Domain (FDTD) Simulation. The software Lumerical FDTD Solutions was implemented to calculate the optical properties of Au nanopyramid arrays, the electric field enhancement, and the quantum efficiency enhancement. A mesh size of 2 nm was used in all simulations. The permittivity of gold used was from Johnson & Christy [50]. The refractive index was set as 1.52 for the glass substrate. A plane wave was used as the input light source. Perfectly Matched Layer boundary conditions were imposed. A gold nanopyramid on glass was modelled to have a base edge length of 140 nm and a height of 250 nm in this work. All the simulations were performed in air, in consistent with experimental conditions.

Detection of GFAP in Blood Plasma. GFAP were spiked into blood plasma with various concentrations of 1.0, 2.0, 5.0, 1.0×10^2, 2.0×10^2, 5.0×10^2, 1.0×10^3, 2.0×10^3, 5.0×10^3, 1.0×10^4, 2.0×10^4, 5.0×10^4, 1.0×10^5 pg/mL, respectively. The detection antibody was labelled with Dylight 755 following the above procedure. The capture antibody was immobilized on the silica-coated Au nanopyramid arrays. Fluorescence detection was conducted in air. For the ELISA test, GFAP were spiked to human blood plasma with concentrations in a range of 0−1000 pg/mL. Following the standard protocol accompanied with the ELISA kit, the optical density of each microplate well was recorded by a BioTek 800 TS absorbance reader.

3. Results and discussions

Operating Principle of Biosensor. Fig. 1 shows the schematic detection principle. A gold nanopyramid array was coated with a thin layer of silica and then functionalized with the capture antibody. In addition, the solution of the detection antibody labelled with Dylight 755 was stored in stock. To realize biosensing, a capture antibody-functionalized Au nanopyramid array was incubated into the analyte solution for 30 min. After rinsing with PBS buffer, the Au nanopyramid array was then incubated into the Dylight-labelled detection antibody solution for additional 30 min. After rinsing with PBS buffer and dried using compressed air, the Au nanopyramid array with the captured analyte and the detection antibody was measured with a portable fluorescence reader.

Characteristics of Gold Nanopyramid Arrays. The as-fabricated Au nanopyramids were arranged hexagonally with a base edge length of 141 nm, as shown in Fig. 2(a) and (b). The plasmonic corner modes were spectrally visible and exhibited as a reflection peak at 735 nm, as shown in Fig. 2(c). FDTD simulation was implemented to calculate the reflection spectra for an Au nanopyramid with a height of 250 nm and a base edge length of 140 nm on glass (Fig. 2(c)). Two orthogonal polarizations were considered during simulation. The overall spectral line shapes were consistent with the experimental one. For one polarization as shown in the purple curve in Fig. 2(c), the longest wavelength peak at about 830 nm came from the plasmonic corner mode, the second longest at about 750 nm from a mixture of the corner and edge modes, and the others from higher-order modes. For other polarization indicated by the orange curve in Fig. 2(c), the major peak at about 775 nm corresponded to a mixture of corner and edge modes. These corner and edge modes were discernible from the calculated electric field distributions, as shown in Fig. S2. It is noted that lack of these fine features on the experimental reflection spectrum can be reasonably ascribed to the rounded corners and edges.

Free-standing gold nanoparticles, gold nanorods, and silver nanoparticles have shown plasmon-enhanced activity in literature. However, free-standing metal nanoparticles tend to aggregate in aqueous sample matrices with high ionic strength, such as blood, serum and plasma. To avoid the particle aggregation problem, the gold nanopyramid array is chosen herein. The gold nanopyramid array chip facilitates stronger light outcoupling owing to the large dimension of an individual nanopyramid as compared to colloidal gold/silver nanoparticles. Especially, the sharp edges and vertices of the pyramids can provide an intense local electromagnetic field for strong excitation enhancement of fluorescence emission. In addition, the size and pitch of the gold nanopyramids in the array pattern can be fabricated using the well-established nanosphere lithography method in a repeatable and controllable manner. Moreover, the gold nanopyramid array also makes it easy to control the separation distance between the fluorophore and the plasmonic nanostructure.

To assess the role of a plasmonic Au nanopyramid array in fluorescence enhancement, 10 μL of 1 μg/mL Dylight 755 was drop-coated on a glass, a gold film, and a gold nanopyramid array substrate coated with a 2.4 nm thick silica layer. Coating a thin layer of silica on the Au nanopyramid array was to minimize the fluorescence quenching due to direct contact between the metallic nanostructure and the fluorophore. Fig. 2(d) shows the fluorescence enhancement factors normalized by the glass substrate. The fluorescence enhancement factors were found to be 0.5 and 8 for the planar Au film and the silica-coated Au nanopyramid array, respectively. It indicates that the fluorescence was partially quenched on the planar Au film but enhanced by 8-fold on the silica-coated Au nanopyramid array. Therefore, the Au nanopyramid array substrates proved effective in amplifying the fluorescence intensity of NIR fluorophores. It is noted that the 8-fold enhancement was obtained when the separation distance between the Au surface and the fluorophore was 2.4 nm.

Detection of TBI Biomarker in Blood Plasma. Various

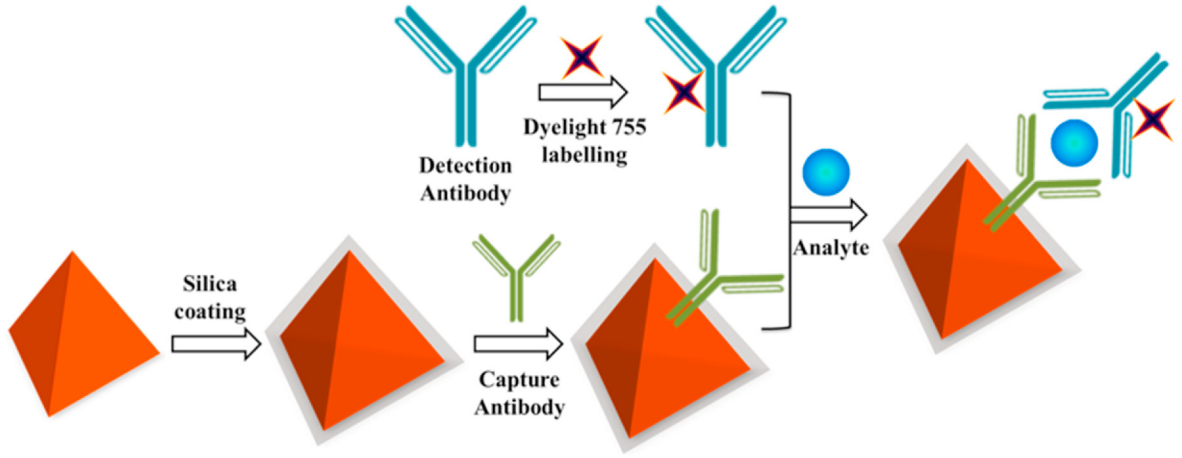

Fig. 1. Operating principle of the plasmonic fluorescent biosensor.

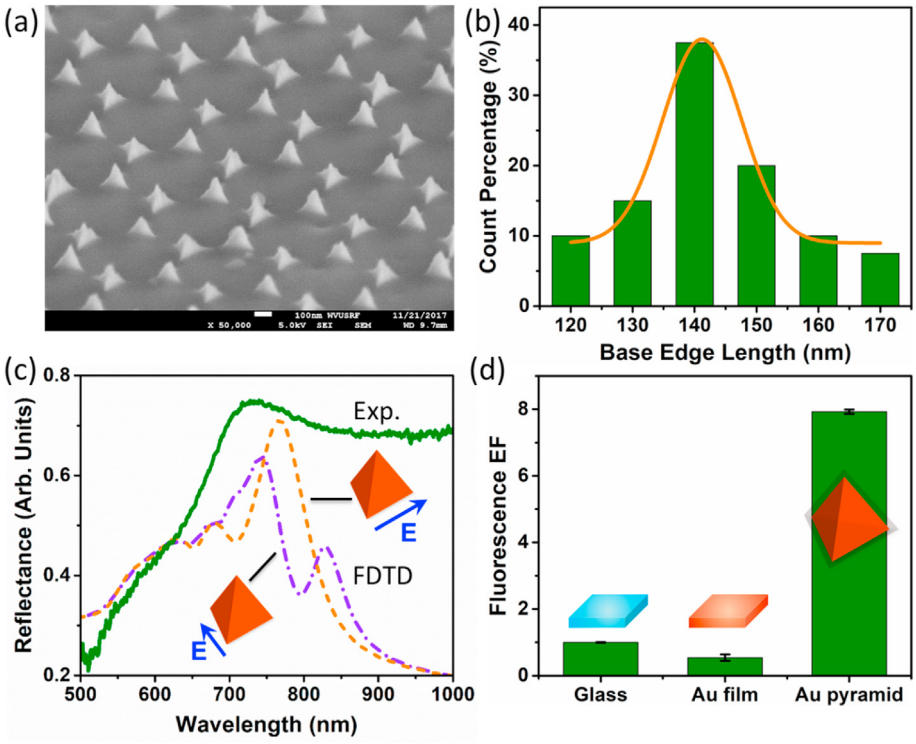

Fig. 2. (a) SEM image of the Au nanopyramid arrays; (b) Statistic analysis of the pyramid base edge length, which was found to be 141 nm based on Gaussian fitting; (c) Comparison of the experimental absorption curve (solid olive curve) and the FDTD-simulated data (dash and dash dotted curves corresponding to two orthogonal polarizations shown as the blue arrows) reflection spectra with an input plane wave incident from the top; (d) Enhancement factor (EF) of the fluorescence intensity of Dylight 755 fluorophore on the Au film and the Au nanopyramid array coated with a 2.4 nm thick silica film as normalized by that on the glass. (For interpretation of the references to colour in this figure legend, the reader is referred to the Web version of this article.)

concentrations of GFAP in blood plasma were tested using the plasmonic fluorescent biosensor, as shown in Fig. 3(a). The glass substrate without the Au nanoarray was used as a control under the same testing conditions. The fluorescence intensity was corrected in reference to the background, that is, it was subtracted by the background signal of the negative control, i.e., the blood plasma without any GFAP biomarker. The resultant data increased with the logarithmic concentration of GFAP for both the sensors and reached a saturated status. The plasmonic fluorescent biosensor displayed a wider linear detection range from 1.0 pg/mL to 500 pg/mL as compared to that (1.0 ng/mL to 10 ng/mL) of the glass substrate, as shown in Fig. 3(b). The linear working concentration range was fitted with equations of $y = 127x+147$, $R^2 = 97\%$ and $y = 90x-182$, $R^2 = 98\%$ for the plasmonic fluorescent biosensor and the glass substrate, respectively. The plasmonic fluorescent biosensor exhibited a larger slope, indicating better sensitivity. The LOD of the plasmonic fluorescent biosensor was 0.6 pg/mL toward GFAP biomarker in blood plasma, which was estimated based on three times signal-to-noise ratio. In contrast, the LOD of the glass substrate sensor was 0.4 ng/mL.

The standard ELISA method was also used to quantify the GFAP spiked in human blood serum. It took about 6 h to perform ELISA measurement. The LOD of the ELISA method was calibrated to be 9.8 pg/mL, which was higher than the LOD (0.6 pg/mL) of our

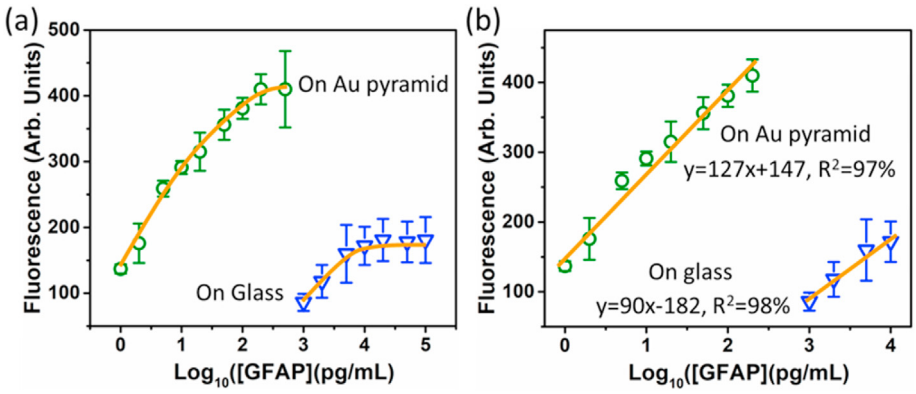

Fig. 3. Detection of Glial Fibrillary Acidic Protein (GFAP) biomarker in blood plasma using based on Au nanopyramid arrays. (a) Performance comparison of the biosensor towards the detection of GFAP in blood plasma on the silica-coated Au nanopyramid arrays and on glass; (b) The linear working range extracted from (a).

plasmonic fluorescent biosensor. Furthermore, the linear working range of the ELISA method (up to 250 pg/mL in Fig. S3(b)) was narrower than that of our plasmonic fluorescent sensor (up to 500 pg/mL). In short, our plasmonic fluorescent biosensor exhibited a shorter measurement time, better sensitivity, and wider linear detection range.

Improvement in LOD was attributed to the excited surface plasmons on the Au nanopyramid arrays, which enhanced fluorescence through combined excitation and emission enhancement mechanism. See detailed numerical simulation in the next section and Supporting Information. As opposed to surface-enhanced Raman scattering (SERS) that requires the Raman molecules to be in close proximity to the plasmonic metallic surface, fluorescence enhancement requires separation of the dye molecules away from the plasmonic metal surface for an optimal separation distance (10–30 nm) to maximize the plasmon enhancement [51,52] In this work, the separation distance between Dylight 755 and the gold nanopyramid array was controlled by two parameters: (i) A thin silica layer is conformally coated on the gold nanopyramid array, which also prevented direct charge transfer, avoiding fluorescence quenching; and (ii) The separation distance was also dependent on the dimension of the capture antibody-antigen-detection antibody complex. As Dylight 755 was labelled on the detection antibody, it was siting on the far end of the complex. The molecular weights of the GFAP antibody and antigen were ~50 kDa and 50 kDa, respectively, which yielded the estimated size of around 3.3 nm for each protein and led to around 9.9 nm-sized complex. Combining both the thin silica layer and the capture antibody-antigen-detection antibody complex, Dylight 755 was estimated to be around 10–13 nm away from the gold nanopyramid array.

Several papers have reported the immunoassays for GFAP detection, as listed in Table S1. Most of those immunoassays have been applied to the PBS buffer sample matrices. In those cases, the GFAP analyte must be extracted from blood to a PBS buffer prior to detection, which requires long time for separation and washing. Our NIR fluorescence biosensor can be directly applied to blood plasma because both the excitation (755 nm) and the emission (775 nm) wavelengths of the NIR fluorophore fall into the first biological transparency window (650–950 nm) [53]. This biosensor also has a much shorter assay time. Furthermore, our NIR fluorescence biosensor exhibits the lowest LOD as compared to the reported immunoassays due to the use of the plasmonic gold nanopyramid nanoarray pattern. In addition, the cut-off value of GFAP for mild TBI is around 60 pg/mL [7,8] which falls within the linear detection range of our plasmonic fluorescent biosensor. This implies that our NIR fluorescence biosensor can be potentially applied for screening of mild TBI by measuring the GFAP biomarker concentration in blood plasma.

FDTD Calculation of Fluorescence Enhancement. To understand the origin of the fluorescence enhancement on the Au nanopyramid array, FDTD calculations were implemented. Detailed description of FDTD calculation can be found in Section S1 in Supporting Information. In our study, the NIR fluorophore used is Dylight 755, which has an intrinsic quantum efficiency of 11.9% [45], among the highest of near-infrared fluorophores. In calculating the excitation enhancement, two orthogonal polarizations were considered for the excitation light source; the transition dipole moment of Dylight 755 perpendicular and parallel to the surface of Au nanopyramid were both considered and averaged to give the quantum efficiency enhancement. A total of 121 points on the plane, which was 10 nm away from the surface of the Au nanopyramid coated with a 2.4 nm silica, were calculated to map the excitation enhancement, the emission enhancement, and the fluorescence enhancement. The calculated results were shown in Fig. 4. Large excitation enhancement was found near and around the pyramid corner area. Nevertheless, the quantum efficiency was found to be reduced at the pyramidal corners, which was attributed to the energy loss associated with the tightly confined local electric field at the corners, giving rise to an enhanced non-radiative decay. Nevertheless, the intense local electric field enhancement effectively compensated the quantum efficiency reduction and ended up enhancing the fluorescence across the entire nanostructure. A maximum fluorescence enhancement factor of 45 was achieved in the polarization direction as specified in Fig. 4(e). In the meanwhile, large fluorescence enhancement factors could be found near and around the pyramid corner area. This indicated that the excitation enhancement was primarily responsible for the fluorescence enhancement on Au nanopyramid arrays.

It is noted that the Au nanopyramid array-based biosensor exhibits almost three orders of magnitude improvement in the LOD as compared to the glass-based counterpart (Fig. 3). This could be attributed to the “sandwich” immuno-construct that helps position the dye molecules at a more favorable distance for higher fluorescence enhancement among other factors, such as the anisotropic pyramidal shape, orientation of antibodies on the pyramidal surface, and the large scattering efficiency of Au nanopyramid arrays [54], all of which may have contributed to the fluorescence enhancement but cannot be reasonably captured by FDTD simulations. In addition, the fluorescence enhancement factor of 45 was calculated for only one dye molecule on the most intense site. In fact, hundreds of molecules are located on different sites over the whole substrate. The collective fluorescence signals from all those

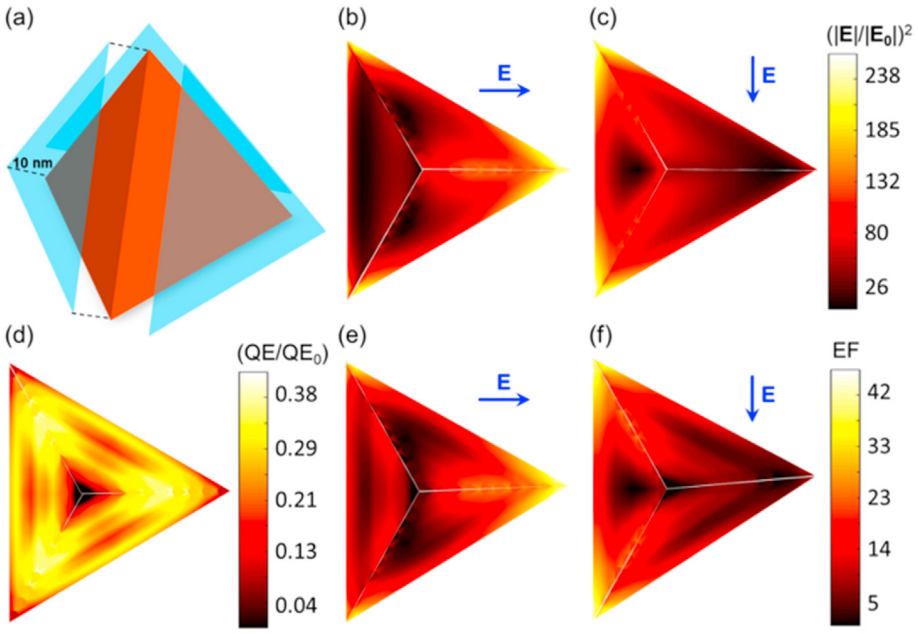

Fig. 4. Calculation of fluorescence enhancement factors. (a) Scheme of the three planes (blue, each being 10 nm away from the surface of Au nanopyramid) on which the local electric field enhancement, quantum efficiency enhancement, and fluorescence enhancement were calculated; (b) and (c) Local electric field enhancement under orthogonal polarizations shown as blue arrows; (d) quantum efficiency enhancement averaged from the dipole perpendicular and parallel to the surface of Au nanopyramid array; (e) and (f) fluorescence enhancement factors under orthogonal polarizations shown as blue arrows. Light was incident from the top. (For interpretation of the references to colour in this figure legend, the reader is referred to the Web version of this article.)

dye molecules were believed to contribute to the enhancement of fluorescence intensity.

4. Conclusions

In summary, a plasmonic fluorescent biosensor was developed for GFAP biomarker detection in blood plasma. Compared to ELISA and other GFAP immunosensors, this plasmonic fluorescent biosensor exhibited a low LOD in blood plasma due to the combined use of the plasmonic nanostructure and the NIR fluorophores in the first biological transparency window. Notably, a portable fluorescence reader was used to record the fluorescence signal from the plasmonic chip instead of a sophisticated spectrofluorometer. Detection of biomarkers with a portable device can enable rapid assessment of TBI in an emergency department or bedside, which will save costs and assist TBI diagnosis, benefit to early medical intervention. FDTD simulation unveiled that fluorescence enhancement was due to the excitation enhancement from the intense local electric field on the sharp corners and edges of the Au nanopyramid array.

CRediT authorship contribution statement

Peng Zheng: Conceptualization, Methodology, Data Collection, Writing – original draft. **Sujan Kasani:** Data Collection, Writing – review & editing. **Weirui Tan:** Data Collection, Validation. **Jennifer Boryczka:** Writing – review & editing. **Xuefei Gao:** Writing – review & editing. **Feng Yang:** Writing – review & editing. **Nianqiang Wu:** Conceptualization, Methodology, Supervision, Writing – review & editing.

Declaration of competing interest

The authors declare that they have no known competing financial interests or personal relationships that could have appeared to influence the work reported in this paper.

Acknowledgment

This work was partially supported by West Virginia University. The use of WVU Shared Research Facilities was acknowledged. Wu is grateful to the support from the endowment fund known as the Armstrong/Siadat Endowed Professorship.

Appendix A. Supplementary data

Supplementary data to this article can be found online at https://doi.org/10.1016/j.aca.2022.339721.

References

[1] C.A. Taylor, J.M. Bell, M.J. Breiding, L.K. Xu, Mmwr. Surveill. Summ. 66 (9) (2017) 1–18.
[2] A.C. Duhaime, J.G. Beckwith, A.C. Maerlender, T.W. McAllister, J.J. Crisco, S.M. Duma, P.G. Brolinson, S. Rowson, L.A. Flashman, J.J. Chu, R.M. Greenwald, J. Neurosurg. 117 (6) (2012) 1092–1099.
[3] R. Mayeux, NeuroRx 1 (2) (2004) 182–188.
[4] K. Strimbu, J.A. Tavel, Curr. Opin. HIV AIDS 5 (6) (2010) 463–466.
[5] L.E. Pelinka, A. Kroepfl, M. Leixnering, W. Buchinger, A. Raabe, H.J. Redl, Neurotrauma 21 (11) (2004) 1553–1561.
[6] H. Zetterberg, D.H. Smith, K. Blennow, Nat. Rev. Neurol. 9 (2013) 201.
[7] L. Papa, S. Silvestri, G.M. Brophy, P. Giordano, J.L. Falk, C.F. Braga, C.N. Tan, N.J. Ameli, J.A. Demery, N.K. Dixit, M.E. Mendes, R.L. Hayes, K.K.W. Wang, C.S. Robertson, J. Neurotrauma 31 (22) (2014) 1815–1822.
[8] L. Papa, L.M. Lewis, J.L. Falk, Z. Zhang, S. Silvestri, P. Giordano, G.M. Brophy, J.A. Demery, N.K. Dixit, I. Ferguson, M.C. Liu, J. Mo, L. Akinyi, K. Schmid, S. Mondello, C.S. Robertson, F.C. Tortella, R.L. Hayes, K.K.W. Wang, Ann. Emerg. Med. 59 (6) (2012) 471–483.
[9] H. Lilja, D. Ulmert, A.J. Vickers, Nat. Rev. Cancer 8 (2008) 268.
[10] J.F. Rusling, C.V. Kumar, J.S. Gutkind, V. Patel, Analyst 135 (10) (2010) 2496–2511.
[11] S.F. Kingsmore, Nat. Rev. Drug Discov. 5 (4) (2006) 310–320.
[12] J. Liu, H. Tang, B. Zhang, X.L. Deng, F.L. Zhao, P. Zuo, B.C. Ye, Y.C. Li, Anal. Bioanal. Chem. 408 (16) (2016) 4287–4295.
[13] T. Wang, Y. Fang, Z.Z. He, Int. J. Electrochem. Sci. 12 (8) (2017) 7341–7350.
[14] S.K. Arya, T.S. Pui, C.C. Wong, S. Kumar, A.R.A. Rahman, Langmuir 29 (22)

(2013) 6770–6777.
[15] W.G. Huang, K. Besar, R. LeCover, P. Dulloor, J. Sinha, J.F.M. Hardigree, C. Pick, J. Swavola, A.D. Everett, J. Frechette, M. Bevan, H.E. Katz, Chem. Sci. 5 (1) (2014) 416–426.
[16] C.D. Abeyrathne, D.H. Huynh, T.T. Lee, T.C. Nguyen, B. Nasr, G. Chana, E. Skafidas, IEEE Sensor. J. 16 (9) (2016) 2898–2905.
[17] J. Song, J. Dailey, H. Li, H.J. Jang, P.F. Zhang, J.T.H. Wang, A.D. Everett, H.E. Katz, Adv. Funct. Mater. 27 (20) (2017) 1606506.
[18] S. Okumoto, A. Jones, W.B. Frommer, Annu. Rev. Plant Biol. 63 (2012) 663–706.
[19] M.C. Morris, M. Blondel, Biotechnol. J. 9 (2) (2014) 171–173.
[20] T. Tamura, I. Hamachi, ACS Chem. Biol. 9 (12) (2014) 2708–2717.
[21] M. Bauch, K. Toma, M. Toma, Q.W. Zhang, J. Dostalek, Plasmonics 9 (4) (2014) 781–799.
[22] A. Ibraheem, R.E. Campbell, Curr. Opin. Chem. Biol. 14 (1) (2010) 30–36.
[23] Y. Haga, H. David Kay, M.A. Tempero, R.K. Zetterman, Clin. Biochem. 25 (4) (1992) 277–283.
[24] O.O. Abugo, R. Nair, J.R. Lakowicz, Anal. Biochem. 279 (2) (2000) 142–150.
[25] A.N. Semenov, B.P. Yakimov, A.A. Rubekina, D.A. Gorin, V.P. Drachev, M.P. Zarubin, A.N. Velikanov, J. Lademann, V.V. Fadeev, A.V. Priezzhev, Molecules 25 (8) (2020) 1863.
[26] H. Zeng, C. MacAulay, D.I. McLean, B. Palcic, J. Photochem. Photobiol. B Biol. 38 (2) (1997) 234–240.
[27] K.G. Chernov, T.A. Redchuk, E.S. Omelina, V.V. Verkhushaa, Chem. Rev. 117 (9) (2017) 6423–6446.
[28] C.H. Tung, R.E. Gerszten, F.A. Jaffer, R. Weissleder, Chembiochem 3 (2–3) (2002) 207–211.
[29] X.X. Cui, Q. Fan, S.J. Shi, W.H. Wen, D.F. Chen, H.T. Guo, Y.T. Xu, F. Gao, R.Z. Nie, H.D. Ford, G.H. Tang, C.Q. Hou, B. Peng, Nanotechnology 29 (20) (2018) 205705.
[30] S. Tsuboi, S. Yamada, Y. Nakane, T. Sakata, H. Yasuda, T. Jin, ECS J. Solid State Sc. 7 (1) (2018) R3093–R3101.
[31] J.R. Lakowicz, Principles of Fluorescence Spectroscopy, third ed., Springer, 1999.
[32] C.-J. Huang, J. Dostalek, A. Sessitsch, W. Knoll, Anal. Chem. 83 (3) (2011) 674–677.
[33] K. Sergelen, S. Fossati, A. Turupcu, C. Oostenbrink, B. Liedberg, W. Knoll, J. Dostálek, ACS Sens. 2 (7) (2017) 916–923.
[34] Z. Zhu, P. Yuan, S. Li, M. Garai, M. Hong, Q.-H. Xu, ACS Appl. Bio Mater. 1 (1) (2018) 118–124.
[35] K.-X. Xie, Q. Liu, X.-L. Song, R.-P. Huo, X.-H. Shi, Q.-L. Liu, Anal. Chem. 93 (8) (2021) 3671–3676.
[36] J.F. Li, C.Y. Li, R.F. Aroca, Chem. Soc. Rev. 46 (13) (2017) 3962–3979.
[37] Y. Fu, J. Zhang, J.R. Lakowicz, J. Am. Chem. Soc. 132 (16) (2010) 5540–5541.
[38] J.R. Lakowicz, K. Ray, M. Chowdhury, H. Szmacinski, Y. Fu, J. Zhang, K. Nowaczyk, Analyst 133 (10) (2008) 1308–1346.
[39] M. Li, S.K. Cushing, N.Q. Wu, Analyst 140 (2) (2015) 386–406.
[40] E. Fort, S. Gresillon, J. Phys. D Appl. Phys. 41 (1) (2007).
[41] P. Anger, P. Bharadwaj, L. Novotny, Phys. Rev. Lett. 96 (11) (2006) 113002.
[42] I.G. Theodorou, Q. Jiang, L. Malms, X. Xie, R.C. Coombes, E.O. Aboagye, A.E. Porter, M.P. Ryan, F. Xie, Nanoscale 10 (33) (2018) 15854–15864.
[43] I.G. Theodorou, Z.A.R. Jawad, Q.F. Jiang, E.O. Aboagye, A.E. Porter, M.P. Ryan, F. Xie, Chem. Mater. 29 (16) (2017) 6916–6926.
[44] F. Shan, D. Su, W. Li, W. Hu, T. Zhang, AIP Adv 8 (2) (2018), 025219.
[45] A.A. Maawy, Y. Hiroshima, S. Kaushal, G.A. Luiken, R.M. Hoffman, M. Bouvet, J. Biomed. Opt. 18 (12) (2013) 126016.
[46] C.L. Haynes, R.P. Van Duyne, J. Phys. Chem. B 105 (24) (2001) 5599–5611.
[47] M. Tabatabaei, A. Sangar, N. Kazemi-Zanjani, P. Torchio, A. Merlen, F. Lagugne-Labarthet, J. Phys. Chem. C 117 (28) (2013) 14778–14786.
[48] P. Zheng, S. Kasani, X. Shi, A.E. Boryczka, F. Yang, H. Tang, M. Li, W. Zheng, D.E. Elswick, N. Wu, Anal. Chim. Acta 1040 (2018) 158–165.
[49] N. Irit, T.A. Bendikov, I. Doron-Mor, Z. Barkay, A. Vaskevich, I. Rubinstein, J. Am. Chem. Soc. 129 (1) (2007) 84–92.
[50] P.B. Johnson, R.W. Christy, Phys. Rev. B 6 (12) (1972) 4370–4379.
[51] B. Peng, Q. Zhang, X. Liu, Y. Ji, H.V. Demir, C.H.A. Huan, T.C. Sum, Q. Xiong, ACS Nano 6 (7) (2012) 6250–6259.
[52] B. Fu, J.D. Flynn, B.P. Isaacoff, D.J. Rowland, J.S. Biteen, J. Phys. Chem. C 119 (33) (2015) 19350–19358.
[53] Y. Hang, J. Boryczka, N.Q. Wu, Chem. Soc. Rev. 51 (2022) 329–375.
[54] P. Zheng, S. Kasani, N.Q. Wu, Nanoscale Horiz. 4 (2) (2019) 516–525.